Physics of Fluids

RESEARCH ARTICLE | OCTOBER 31 2022

Investigation of the characteristics and mechanisms of the layer inversion in binary liquid–solid fluidized beds with coarse particles

Wan-Long Ren (任万龙); Yan Zhang (张岩); Xu-Hui Zhang (张旭辉) ✉; ... et. al

Check for updates

Physics of Fluids 34, 103325 (2022)
https://doi.org/10.1063/5.0111157

CrossMark

View Online

Export Citation

Articles You May Be Interested In

An optimized Eulerian–Lagrangian method for two-phase flow with coarse particles: Implementation in open-source field operation and manipulation, verification, and validation

Physics of Fluids (November 2021)

Simulation of the Flow and Segregation of Particle Mixtures in Liquid Fluidization

AIP Conference Proceedings (June 2009)

Theoretical study of fluidization and heat transfer on fluidized bed coffee roaster

AIP Conference Proceedings (April 2019)

Downloaded from http://pubs.aip.org/aip/pof/article-pdf/doi/10.1063/5.0111157/16578096/103325_1_online.pdf

AIP Publishing

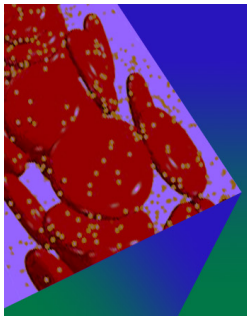

Physics of Fluids

Special Topic: Flow and Forensics

Submit Today!

AIP Publishing

Physics of Fluids ARTICLE scitation.org/journal/phf

Investigation of the characteristics and mechanisms of the layer inversion in binary liquid–solid fluidized beds with coarse particles

Cite as: Phys. Fluids **34**, 103325 (2022); doi: 10.1063/5.0111157
Submitted: 18 July 2022 · Accepted: 29 September 2022 ·
Published Online: 31 October 2022

View Online Export Citation CrossMark

Wan-Long Ren (任万龙),[1,2] Yan Zhang (张岩),[1] Xu-Hui Zhang (张旭辉),[1,2,a)] and Xiao-Bing Lu (鲁晓兵)[1,2]

AFFILIATIONS

[1]Institute of Mechanics, Chinese Academy of Sciences, Beijing 100190, China
[2]School of Engineering Science, University of Chinese Academy of Sciences, Beijing 100049, China

[a)]Author to whom correspondence should be addressed: zhangxuhui@imech.ac.cn

ABSTRACT

This paper adopts an optimized Euler–Lagrange method proposed in our previous work to study the characteristics and formation mechanisms of layer inversion in binary liquid–solid fluidized beds (LSFBs) with coarse particles. The LSFBs are formed in a cylindrical pipe with a diameter of 50 mm and a length of 0.6 m and consist of two species of coarse particles with different sizes: 6 mm glass spheres (species 1) and 10 mm glass spheres (species 2) with the particle density of 2600 kg/m^3. First, the characteristics of the layer inversion of LSFBs with coarse particles are qualitatively analyzed. The positions of species 1 and species 2 are converted during layer inversion. Second, the changes in the trajectory and volume fraction of two species of particles are quantitatively investigated. Finally, the formation mechanisms of layer inversion with coarse particles are analyzed. The results show that the relative magnitude of the fluid–solid interaction force and the gravity is the main reason for determining the layer inversion of binary coarse particles of different sizes. The collision force is to balance the net force of the particle–fluid interaction force and the net gravity, so that the fluidized bed is in relative equilibrium. In addition, through the analysis of the evolution of the network of contact forces, the constraint of the wall on coarse particles is discussed during the layer inversion.

Published under an exclusive license by AIP Publishing. https://doi.org/10.1063/5.0111157

I. INTRODUCTION

Fluidization of liquid–solid fluidized beds (LSFBs) is the process in which solid particles are suspended in the ascending fluid. Due to the characteristics of uniform dispersion of solid particles, good fluid–solid contact, excellent heat and mass transfer performance, and the fast reaction rate, LSFBs have been frequently used in energy, chemical, metallurgical, and other industries in the early stage.[1,2] In recent years, with the development of LSFBs research, more attention has been paid to environmental, food, and biochemical industries. In industrial production, segregation is a popular phenomenon in fluidization of binary LSFBs due to the influence of particle size, density, shape, or other factors. It can be used to separate materials and affect the quality of products.[3,4] Therefore, it is of great significance to investigate layer inversion in the particle segregation process for the application of LSFBs in solid classifiers or biochemical reactions.[5]

Layer inversion occurs in binary LSFBs where the sizes of the two species of particles are different. Compared to the minimum fluidization velocity, there are two separated layers at lower liquid velocity, with smaller particles (species 1) on the bottom and larger particles (species 2) on the overlying layer. When the liquid velocity is slightly higher, the particles of species 1 travel through the top species 2, and the particles of species 2 are placed on the bottom. The phenomenon of layer inversion in LSFBs was first reported by Hancock.[6] Subsequently, a large number of researchers[7–12] conducted experimental research, theoretical modeling, and numerical simulation. Moritomi *et al.*[13] proposed that the layer inversion could be realized by changing the liquid velocity or varying the solids composition of the beds at a given liquid velocity. Some models were proposed to predict layer inversion phenomenon in fluidized beds. The serial model was reported by Epstein and LeClair.[14] He proposed that the segregation depended on the difference the bulk densities of two species of particles. Based on the Richardson–Zaki correlation,[15] the quantitative expressions for the layer inversion velocity were obtained. Hu[16] improved the prediction model of layer inversion velocity proposed by Epstein and LeClair[14] from the force balance and compared the model results with the experiments of Moritomi *et al.*[13] However, the layer inversion velocity predicted by the serial model only depends on the

Published under an exclusive license by AIP Publishing

Downloaded from http://pubs.aip.org/aip/pof/article-pdf/doi/10.1063/5.0111157/16578096/103325_1_online.pdf

particle and liquid properties. Therefore, it cannot predict the overall solids composition of the binary LSFBs.

The property averaging model based on beds expansion of the binary mixture was proposed by Gibilaro *et al.*,[17] which introduced mean particle properties to predict the solids composition of the bottom mixing layer. When the solid component of the bottom mixing layers corresponded to overall solids composition, the binary LSFBs consisted of a single mixing zone. The liquid velocity corresponded to the layer inversion velocity in the case. Asif[18] proposed a hybrid model including the serial model and the property averaging model based on the previous research results and modified "the property averaging model" by using the correlations of Khan and Richardson.[19]

More recently, the particle segregation model (PSM) method proposed by Di Maio and Di Renzo[10] could predict the segregation direction and the layer inversion voidage by providing information about solids properties and fluidized beds composition. The reliability of the PSM model was verified by comparing the measured solid concentration in the experimental and the inversion voidage with the PSM predictions.[20] Rim *et al.*[21] investigated layer inversion in binary LSFBs when gas and liquid coexisted. They found that layer inversion velocity decreased with the increase in gas velocity.

The ratio of particle diameter to pipe diameter in LSFBs was small. However, the particles are often coarse in some projects. The coarse particles in the pipe refer to the ratio of particle size to pipe diameter greater than 0.1, such as in deep-sea mining.[22] Particles of species 1 often pass-through particles of species 2 during transportation, so that the local concentration of particles in the pipe is higher, which leads to pipe blockage. Therefore, the study on the characteristics and formation mechanisms of layer inversion in LSFBs with coarse particles can provide theoretical guidance for preventing pipe blockage. Viggiano *et al.*[23] carried out two-phase flow loop experiments using the advanced x-ray system. The local phase fraction of the pipeline cross-section was measured, and the data were carried out to understand the phase fraction characteristics of the dispersed and slug flows. In addition, Ali *et al.*[24] also used an x-ray system to obtain cross-sectional phase fractions of two-phase regimes and revealed the flow structures of dispersed and slug flows based on clustering algorithms. They also investigated the two-phase flow regimes by implementing a system identification approach to obtain reduced-order models that accurately captures the flow dynamics.[25]

Since the last decade, numerical simulation has been widely used in the LSFBs. Detailed information is difficult to obtain from the experiment, such as the local solid/liquid volume concentration, solid/liquid spatial distribution, and force information. The information can help understand the characteristics of layer inversion in binary LSFBs, which makes numerical simulation a possible source of data. Generally speaking, there are two numerical methods to simulate multiphase flow: one is the Euler–Euler method,[26–28] and the other is the Euler–Lagrange method.[29–34] In the Euler–Euler method, particle and fluid phases are regarded as a continuum, but discrete characteristics of particles cannot be showed. In the Euler–Lagrange method, the particle phase is regarded as dispersed phase to obtain the local motion characteristics of the particles. Therefore, the Euler–Lagrange method is applied to the investigation of characteristics of layer inversion by more researchers.[35–39]

Viggiano *et al.*[40] proposed a stochastic model for Lagrangian velocity and acceleration considering the effects of particle inertia. In addition, they also proposed a modeling technique for single inertial particle statistics based on a filtering approach for the Lagrangian fluid velocity and introduced an effective particle response time τ_p^* and an effective Stokes number, which improved the application scope of the model and greatly expanded the Lagrangian models.[41] Malone *et al.*[42] found the segregation of the different particle species based on the computational fluid dynamics–discrete element method (CFD–DEM). Zhou and Yu[43] investigated the potential mechanisms of layer inversion by analyzing the particle–particle interaction force and particle–liquid interaction force. Molaei *et al.*[44] gave the prediction formula of inversion velocity using the CFD–DEM method. However, they studied fine particles. The classical experimental and numerical simulation data of binary particle separation in liquid–solid fluidized beds are added in Table I.

For coarse particles, Cúñez and Franklin[45] investigated experimentally and numerically the characteristics of layer inversion. The solid–liquid fluidized beds consisted of alumina beads with $d_2 = 6$ mm (species 2) and aluminum beads with $d_1 = 4.8$ mm (species 1) in a cylindrical pipe with a diameter of 25.4 mm. The D/d was 4.23 and 5.29 for species 1 and species 2, respectively, where D/d was the ratio of the pipe diameter to particle diameter. Finally, they gave the characteristic time for layer inversion by considering the profiles of volume fraction. However, they did not study the formation mechanisms of layer inversion in binary LSFBs. Cúñez and Franklin[46] also experimentally investigated the crystallization and jamming with size ratios and density ratios of different coarse particles.

Although a lot of research has been carried out on binary LSFBs, there are few studies on liquid–solid fluidized beds with coarse particles, and the formation mechanisms of layer inversion are not well understood. The mesh size is required to be more than three times larger than the particle diameter to guarantee simulation accuracy in the general CFD–DEM method.[47] Due to the limitation of cell size, the coarse particle size needs to be larger than the cell size, but the conventional numerical model cannot meet the requirements. In our previous work, an optimized Euler–Lagrange method based on the open source platform Open Field Operation And Manipulation (OpenFOAM) has been applied to solve the problem, which has been verified by experiments.[48] We also investigated the transportation behavior of coarse particles in hydraulic lifting using the method in deep-sea mining.[22] Now, the method has been implemented into the open source platform through the computational fluid dynamics/discrete element method (CFDEM).[49,50] The CFDEM combines OpenFOAM for the CFD module and lammps improved for general granular and granular

TABLE I. The classical experimental and numerical simulation data of binary particle separation in LSFBs.

Authors	D (mm)	d_2 (mm)	d_1 (mm)	d_2/D	d_1/D
Moritomi *et al.*[13]	50	0.775	0.163	0.016	0.003
Epstein and LeClair [14]	50.8	3.15	2.05	0.06	0.04
Asif[18]	60	2.76	0.463	0.046	0.008
Zhou and Yu [43]	150	0.78	0.19	0.005	0.001
Molaei *et al.*[44]	10	0.778	0.193	0.078	0.020
Cúñez and Franklin [45]	25.4	6	4.8	0.236	0.189
Xie *et al.*[39]	50	4	1	0.08	0.02

Downloaded from http://pubs.aip.org/aip/pof/article-pdf/doi/10.1063/5.0111157/16578096/103325_1_online.pdf

Published under an exclusive license by AIP Publishing

heat transfer simulations (LIGGGHTS)[51] for the DEM module, which significantly simplifies the algorithm and accelerates the operation speed. It provides an effective way for the simulation of large-scale coarse particles in complex industrial projects.

The aim of this work is to investigate the characteristics and the formation mechanisms of the layer inversion phenomenon of binary coarse particles in a liquid–solid fluidized bed based on an optimized Euler–Lagrange method proposed by us.[48] The influence of the pipe wall on coarse particle is also discussed.

The remainder of this paper is as follows. In Sec. II, this part simply summarizes the governing equations. In Sec. III, computational settings are described. In Sec. IV, this section focuses mainly on model validation, the characteristics of layer inversion, and force analysis. Finally, conclusions are drawn in Sec. V.

II. MODEL DESCRIPTION

A. Solid phase equations

The motion of each particle in the fluid mainly includes the translation and rotation. The driving force of each particle movement comes from the drag force, the pressure gradient force, and the particle–particle/wall interaction force. Based on the Newton's second law, the motion equation of each particle can be expressed as[52,53]

$$m_p \frac{d\mathbf{u}_p}{dt} = \mathbf{F}_{fp} + \mathbf{F}_{col} + m_p \mathbf{g}, \tag{1}$$

$$I_p \frac{d\boldsymbol{\omega}_p}{dt} = \mathbf{M}, \tag{2}$$

where m_p, $\mathbf{u}_p$, $I_p = m_p d^2/10$, and $\boldsymbol{\omega}_p$ are the particle mass, translation velocity, inertia moment, and angular velocity of particles, respectively. d is the particle diameter. $\mathbf{F}_{fp}$ is the particle–fluid interaction force, and $\mathbf{g}$ is the acceleration of gravity. $\mathbf{M}$ represents friction torque. $\mathbf{F}_{col}$ is the contact force. The contact force is decomposed into normal contact force $\mathbf{F}_{cn}$ and tangential contact force $\mathbf{F}_{ct}$, which is calculated based on the soft ball model.[54,55]

The normal contact force $\mathbf{F}_{cn}$ is defined as

$$\mathbf{F}_{cn,ij} = \left(k_n \delta_{nij}^{\frac{3}{2}} - \eta_n \mathbf{u}_{ij} \cdot \mathbf{n}_{ij}\right)\mathbf{n}_{ij}. \tag{3}$$

The tangential component $\mathbf{F}_{ct}$ is defined as

$$\mathbf{F}_{ct,ij} = \begin{cases} k_t|\boldsymbol{\delta}_t| > \mu \mathbf{F}_{ct,ij}, & -\mu|\mathbf{F}_{ct,ij}|\dfrac{\mathbf{v}_{slipij}}{|\mathbf{v}_{slipij}|}, \\ k_t|\boldsymbol{\delta}_t| \le \mu \mathbf{F}_{ct,ij}, & -k_t\boldsymbol{\delta}_t - \eta_t \mathbf{v}_{slipij}, \end{cases} \tag{4}$$

where $\mathbf{F}_{cn,ij}$ and $\mathbf{F}_{ct,ij}$ are the contact force (normal and tangential component) of particle i to particle j, respectively. n and t represent the normal and tangential directions, respectively, and k_t, η_t, and $\boldsymbol{\delta}_t$ are the spring coefficient, the damping coefficient, and the particle deformation or particle overlaps, respectively. μ is the friction coefficients.

B. Fluid phase equations

The fluid field information is obtained by solving the average incompressible Navier–Stokes (N–S) equation,[56] as follows:

$$\frac{\partial \varepsilon_f}{\partial t} + \nabla \cdot (\varepsilon_f \mathbf{u}_f) = 0, \tag{5}$$

$$\frac{\partial(\varepsilon_f \mathbf{u}_f)}{\partial t} + \nabla \cdot (\varepsilon_f \rho_f \mathbf{u}_f \mathbf{u}_f) = \varepsilon_f \nabla P + \nabla \cdot (\varepsilon_f \boldsymbol{\tau}_f) + \varepsilon_f \rho_f \mathbf{g} + \mathbf{f}_{pf}, \tag{6}$$

where $\mathbf{u}_f$ is the liquid velocity, ε_f is the volume fraction of the fluid, P is the fluid pressure, ρ_f is the fluid density, $\boldsymbol{\tau}_f$ is the shear stress tensor of the fluid, $\mathbf{g}$ is the gravity acceleration, and $\mathbf{f}_{pf}$ is the momentum exchange term of the interaction between particles and the fluid. The viscous stress tensor of the fluid is expressed as

$$\boldsymbol{\tau}_f = \nu_f\left(\nabla \mathbf{u}_f + \nabla \mathbf{u}_f^T\right) - \frac{2}{3}\nu_f \nabla \cdot \mathbf{u}_f \mathbf{I}, \tag{7}$$

where ν_f is the fluid viscosity and $\mathbf{I}$ is the unit matrix. The Reynolds-averaged Navier–Stokes (RANS) k–ε model is used.[48]

C. Fluid–solid interaction

The forces on particles mainly include the drag force, the lift force (the Magnus force and the Saffman force), the pressure gradient force, the virtual mass force, and the Basset force.[57] The forces of particles mainly consider the drag force and the pressure gradient force in the LSFBs with coarse particles,[58]

$$\mathbf{F}_{pf} = \mathbf{F}_d + \mathbf{F}_p + \mathbf{F}_l, \tag{8}$$

where $\mathbf{F}_{pf}$ is the fluid–solid interaction force, $\mathbf{F}_d$ is the drag force, and $\mathbf{F}_p$ is the pressure gradient force. In addition, we also consider the lift force $\mathbf{F}_l$.[57] In this work, the Gidaspow model is applied to calculate the drag force,[59] and the Gidaspow model combines the Ergun model[60] and the Wen–Yu model,[61]

$$\mathbf{F}_d = \frac{V_p \beta}{(1-\varepsilon_f)}(\mathbf{u}_f - \mathbf{u}_p), \tag{9}$$

$$k_d = \begin{cases} \varepsilon_f < 0.8 & V_p\left(150\dfrac{(1-\varepsilon_f)}{\varepsilon_f}\dfrac{\mu_f}{d^2} + 1.75\dfrac{\rho_f|\mathbf{u}_f - \mathbf{u}_p|}{d}\right), \\ \varepsilon_f \ge 0.8 & V_p\dfrac{3}{4}C_d\dfrac{\rho_f|\mathbf{u}_f - \mathbf{u}_p|}{d}\varepsilon_f^{-2.65}, \end{cases} \tag{10}$$

$$C_d = \begin{cases} Re < 1000 & \dfrac{24(1+0.15Re^{0.687})}{Re}, \\ Re \ge 1000 & 0.424, \end{cases} \tag{11}$$

$$Re = \frac{\rho_f|\mathbf{u}_f - \mathbf{u}_p|d}{\mu_f}, \tag{12}$$

where β is the momentum transfer coefficient between different phases, $\mathbf{u}_f$ is the liquid velocity at the particle position, $\mathbf{u}_p$ is the particle velocity, V_p is the particle volume, C_d is the drag coefficient, Re is the relative particle Reynolds number, and μ_f is the viscosity of the fluid phase.

The pressure gradient force is the force on particles due to the existence of pressure gradient in the fluid field, which can be expressed as

$$\mathbf{F}_p = -\left(\frac{1}{6}\pi d^3\right)\nabla P, \tag{13}$$

where ∇P is the gradient of pressure along the $\mathbf{x}$ direction. This force is actually the buoyancy of particles in a static fluid considering gravity.

The lift force is that particles are subjected to in the fluid perpendicular to the direction of particle–fluid relative motion. The lift force

Downloaded from http://pubs.aip.org/aip/pof/article-pdf/doi/10.1063/5.0111157/16578096/103325_1_online.pdf

Published under an exclusive license by AIP Publishing

mainly refers to Magnus force due to particle rotation.[62] The Magnus force can be calculated by the following formula:

$$\mathbf{F}_{\mathrm{l}} = \frac{\pi}{8} d^3 \rho_{\mathrm{f}} \omega_{\mathrm{p}} (\mathbf{u}_{\mathrm{f}} - \mathbf{u}_{\mathrm{p}}), \tag{14}$$

where $\mathbf{F}_{\mathrm{l}}$ is the lift force and ω_{p} is the angular velocity of spin of the particles.

D. Virtual mass distribution function (VMDF)

The problem of LSFBs involves liquid–solid coupling. The particles and fluid are coupled by the particle volume fraction and the momentum exchange term. The data interchange between the Eulerian and Lagrangian fields is necessary in the coupling process. The Virtual Mass Distribution (VMDF) function for coarse particles is used to resolve the condition that the particle size is larger than the cell size. The VMDF of coarse particles is shown in Fig. 1. The virtual density distribution (VDDF) function is defined as

$$m_V(\gamma) = \frac{4}{3}\pi R^3 \rho_{\mathrm{d}} \varphi(\gamma, \tau), \tag{15}$$

$$M_V(\infty) = \frac{4}{3}\pi R^3 \rho_{\mathrm{d}} = M_T(\infty), \tag{16}$$

where $m_V(\gamma)$ is the VDDF and $M_V(\gamma)$ is the VMDF.

The particle volume fraction field at cell I relating to the particle p locating at cell J with any mesh scale can be written as

$$\begin{aligned}\varepsilon_{\mathrm{p}}(\mathbf{x}_I) &= \frac{1}{V_{\mathrm{cell}}(J)} \int_{|\gamma| \in V_{\mathrm{cell}}(I)} \frac{1}{\rho_{\mathrm{p}}} m_{\mathrm{V}}(\gamma) \mathrm{d}\gamma \\ &= \int_{|\gamma| \in V_{\mathrm{cell}}(I)} \frac{4}{3} \frac{\pi R^3}{V_{\mathrm{cell}}(J)} \frac{1}{(4\pi\tau)^{\frac{3}{2}}} \exp\left(-\frac{\gamma^2}{4\tau}\right) \mathrm{d}\gamma \\ &= \int_{|\gamma| \in V_{\mathrm{cell}}(I)} \frac{\varepsilon_{\mathrm{p,PCM}}(\mathbf{x}_J)}{(4\pi\tau)^{\frac{3}{2}}} \exp\left(-\frac{\gamma^2}{4\tau}\right) \mathrm{d}\gamma\,,\end{aligned} \tag{17}$$

where $\mathbf{x}_I$ and $\mathbf{x}_J$ are the location vectors of the center points of cell I and J, respectively, $V_{\mathrm{cell}}(I)$ and $V_{\mathrm{cell}}(J)$ are the volumes of cell I and J, respectively, and $\varepsilon_{\mathrm{p,PCM}}(\mathbf{x}_J)$ is the volume fraction of particles in cell J. Based on the Green's function, Eq. (17) is the solution of the following equation:

$$\begin{cases} \dfrac{\partial \varphi(\boldsymbol{\beta}, \tau)}{\partial \tau} = \nabla^2 \varphi(\boldsymbol{\beta}, \tau), \\ \varphi(\boldsymbol{\beta}, \tau)|_{\tau=0} = \varepsilon_{\mathrm{p,PCM}}(\mathbf{x}_J)\delta(\mathbf{x}_{\mathrm{J}}). \end{cases} \tag{18}$$

Similar to the particle volume fraction, the solid–liquid momentum exchange term of coarse particles is dispersed into the surrounding cells for the solid–liquid momentum exchange term $\mathbf{f}_{\mathrm{dl}}$,

$$\mathbf{f}_{\mathrm{dl}}(\varsigma) = \mathbf{f}_{\mathrm{dl,PCM}}(\mathbf{x}) \varphi(\mathbf{x} - \varsigma, \tau), \tag{19}$$

where ς is the position vector of any point in the fluid field, $\mathbf{f}_{\mathrm{dl}} (\mathbf{f}_{\mathrm{dl}} = \mathbf{f}_{\mathrm{d}} + \mathbf{f}_{\mathrm{l}})$ is the solid–liquid momentum exchange term, and $\mathbf{f}_{\mathrm{dl,PCM}}$ is based on the particle volume fraction in the cell $\mathbf{x}$. Equation (19) can also be achieved by solving the following equation:

$$\begin{cases} \dfrac{\partial \mathbf{f}_{\mathrm{dl,PCM}}}{\partial \tau} = \nabla^2 \mathbf{f}_{\mathrm{dl,PCM}}, \\ \mathbf{f}_{\mathrm{dl,PCM}}|_{\tau=0} = \mathbf{f}_{\mathrm{dl,PCM}}(\mathbf{x})\delta(\mathbf{x}), \end{cases} \tag{20}$$

where $\mathbf{x}$ is the center of the containing cell of the particle. More details about VMDF can be found in Ref. 48.

III. COMPUTATIONAL SETTINGS

As shown in Fig. 2, the LSFB is formed in a cylindrical pipe with a diameter of 0.05 m and a height of 0.6 m in this study. ANSYS ICEM is used for geometric modeling and cell generation. The geometric domain of the pipe is divided into "O" type, and the computational domain is divided into a hexahedral mesh with a total number

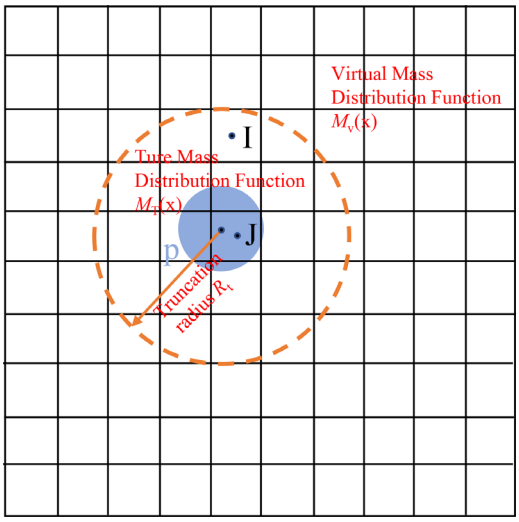

FIG. 1. The virtual mass distribution function.

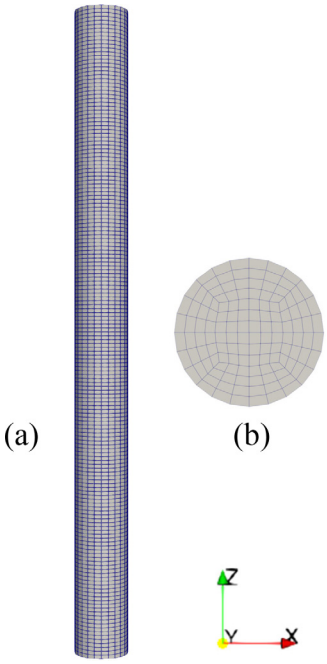

FIG. 2. Computational geometry: (a) side view and (b) bottom view.

Downloaded from http://pubs.aip.org/aip/pof/article-pdf/doi/10.1063/5.0111157/16578096/103325_1_online.pdf

Published under an exclusive license by AIP Publishing

of 32 928 cells. The pipe has three boundaries, namely, the inlet, the outlet, and the wall. For fluid (continuous phase), the liquid velocity is a given value at the inlet. The liquid velocity is 0 m/s at the wall. The atmospheric pressure is assumed at the outlet. For particles (discrete phase), the velocity is 0 m/s when particles initially enter the pipe.

The LSFBs consist of 6 mm glass spheres (species 1) and 10 mm glass spheres (species 2). Particles of species 1 are at the bottom of the pipe, and particles of species 2 are on the overlying layer. In the initial condition, particles freely settle down under gravity. Then, the packed bed is fluidized from the bottom of the pipe at a pre-set liquid velocity. The initial state of particles is shown in Fig. 3. Parameters used in the numerical simulation of the fluidized beds are shown in Table II.

The particle motion is solved in DEM module, and the fluid field is in the CFD module. The time steps of DEM module (t_{DEM}) and CFD module (t_{CFD}) are generally different. Li *et al.*[63] suggested a critical time step based on the time of Rayleigh wave propagating along the average particle radius $\bar{R}$ for particles. The time step is calculated by the following equation:

$$\Delta t_{\mathrm{DEM}} = \frac{\pi \bar{R}}{0.163\nu + 0.8766}\sqrt{\frac{2\rho_{\mathrm{p}}(1+\nu)}{E}}, \tag{21}$$

where ν is Poisson's ratio, E is Young's modules, and ρ_{p} is the particle density.

The cases with and without boundary layer are compared. First, particles with a diameter of 10 mm are freely packed at the bottom of the pipe, and the parameter settings are the same as the standard case in this paper (Table II). The particles begin to fluidize under the action of the inlet velocity of the pipe. In Fig. 4(a), we compare the variation of particle volume fraction along the radial direction of the pipe at the cross section of the bed height of 0.085 m. The average particle–fluid interaction force over time also is compared in Fig. 4(b). The results show that the numerical results with or without boundary layer are close in this paper. However, the time cost of calculation increases significantly in the case of boundary layer. Therefore, considering the computational cost and results, this paper chooses the geometric model without the boundary layer.

In order to verify the influence of mesh size on the calculation results, six sets of meshes with different sizes are calculated. The detailed parameters of the meshes are shown in Table III. By placing different numbers of nodes in the diameter direction and length direction of the pipe, different sizes of meshes are obtained, and the mesh division forms are the same. The parameters of the case are the same as those of the standard case (Table II). Figure 5 shows the comparison of the minimum fluidization velocity of 10 mm particles under different size meshes and the change of the average local volume fraction of particles. Comparing the results of different mesh calculations, the results of radial mesh nodes not less than 15 are basically close. Considering the computational efficiency and accuracy, the mesh with 15 radial mesh nodes is selected for cases of the article.

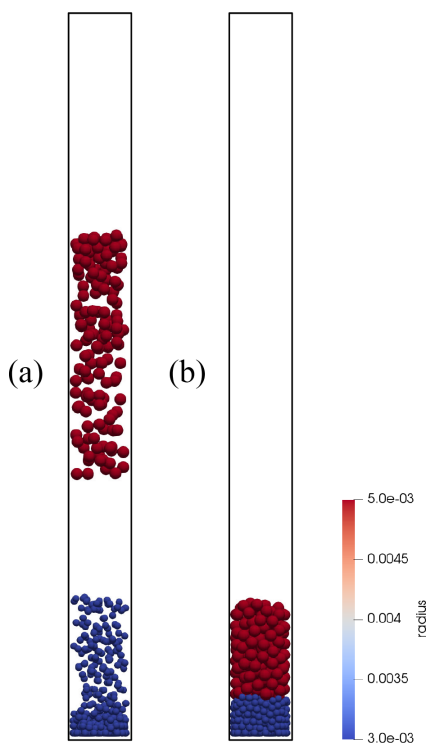

FIG. 3. Initial state of particles: (a) free fall of species 1 and 2 and (b) initial accumulation of species 1 and 2. Red color corresponds to species 2 and blue color corresponds to species 1.

TABLE II. Parameters used in the numerical simulation of binary liquid–solid fluidized beds with coarse particles.[22,63]

Parameters	Values
Geometry of the vertical pipe	
Diameter	50 mm
Length	0.6 m
Particle properties	
Density ρ_{p}	2600 kg/m^3
Species 1 d_1	6 mm
Species 2 d_2	10 mm
Young's modulus E	1.0×10^8 Pa
Poisson's ratio ν	0.23
Coefficient of restitution for particle–particle/wall $\alpha/\alpha_{\mathrm{w}}$	0.5/0.5
Coefficient of friction for particle–particle/wall μ/μ_{w}	0.5/0.5
Water properties	
Density ρ_{f}	1000 kg/m^3
Viscosity μ_{f}	1.0×10^{-3} Pa s
Velocity u_0	0.10–0.20 m/s
Simulation setup	
Number of species 1 N_1	300
Number of species 2 N_2	150
CFD time step	5.0×10^{-4} s
DEM time step	1.0×10^{-5} s
Simulation time	0–30 s

Downloaded from http://pubs.aip.org/aip/pof/article-pdf/doi/10.1063/5.0111157/16578096/103325_1_online.pdf

Published under an exclusive license by AIP Publishing

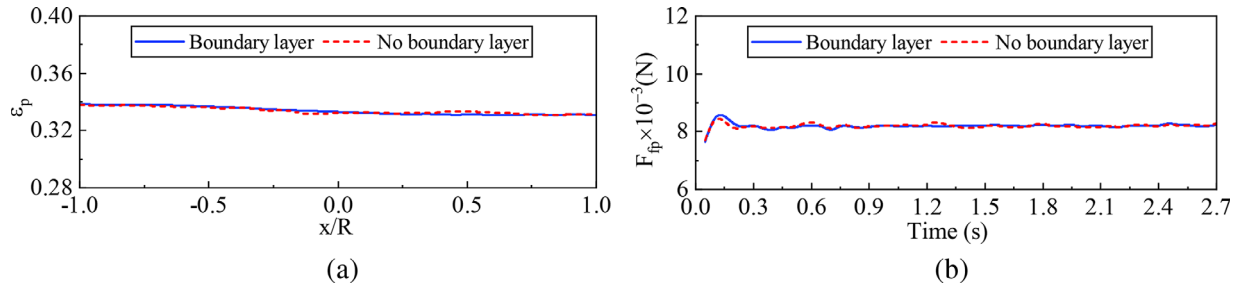

FIG. 4. The case verification with and without the boundary layer: (a) the variation of particle volume fraction along the radial direction and (b) the average particle–fluid interaction forces over time.

TABLE III. The detailed mesh size used in the numerical simulation.

Case	The number of mesh nodes (radial × circumferential × axial)	Mesh number
1	11 × 21 × 121	12 000
2	15 × 29 × 169	32 928
3	16 × 31 × 181	40 500
4	18 × 35 × 205	58 956
5	21 × 41 × 241	96 000
6	24 × 47 × 277	146 004
7	26 × 51 × 301	187 500

IV. RESULTS AND DISCUSSION

A. Model validation

Now an optimized Euler–Lagrange method has been successfully implanted into the CFDEM platform (CoarseDPMFoam). In this part, we simply verify the CoarseDPMFoam solver by testing the minimum fluidization velocity of coarse particles with different densities. First, a pipe with a diameter of 50 mm and a height of 0.6 m is built. Second, 150 coarse particles with a diameter of 10 mm are freely stacked in the pipe. The density of particles is set to 1100, 1400, 1700, 2000, 2300, and 2600 kg/m^3, while the water density is 1000 kg/m^3 with a viscosity of 0.001 kg/(m s). Finally, the linear variation velocity of liquid velocity of 0–0.1 m/s is set at the inlet of the pipe. The pressure drop between the inlet and the top of the granular layer is calculated. When the pressure drop is fundamentally stable, the velocity is determined as the minimum fluidization velocity of the granular layer. Theoretical value of minimum fluidization velocity of the granular layer is calculated using the Ergun formula and compared to the results of the numerical simulation.[60] The Ergun formula is shown in the Appendix.

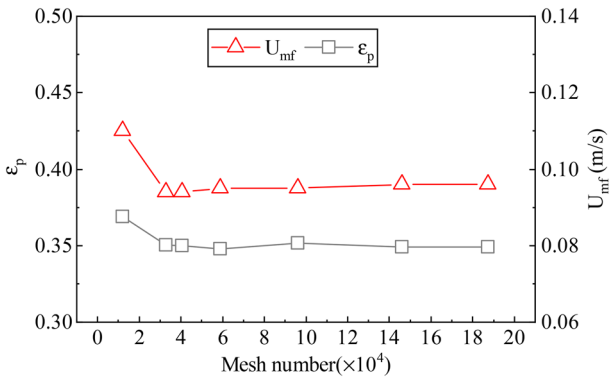

FIG. 5. Mesh independence investigation under meshes of different sizes: the red line represents minimum fluidization velocity (right) and the gray line represents the average local volume fraction of particles (left).

As shown in Fig. 6(a), we take the particle density of 1700 kg/m^3 as an example. The minimum fluidization velocity is 0.0615 m/s when the pressure drop curve is fundamentally stable. The minimum fluidization velocity calculated by Ergun formula is 0.0601 m/s. The minimum fluidization velocity for other density particles is similarly determined. The final results are shown in Fig. 6(b).

The comparison with the experimental results of the literature is introduced:[64] 120 g species 1 with the diameter 8 mm and species 2 with the diameter 3 mm is set, while five superficial velocities (0.141, 0.149, 0.156, 0.163, and 0.170 m/s) are applied in the inlet of pipe. The particle density is 2230 kg/m^3, while the water density is 1000 kg/m^3 with a viscosity of 0.001 kg/(m s). The geometric mesh is the same as the standard case in this paper (Fig. 2). Figure 7 shows the comparison between the expansion height of the fluidized bed after equilibrium and the experimental results.

B. The characteristics of layer inversion

In this paper, the simulated time (0–30 s) is normalized by the relaxation time of species 2[65,66] ($\tau_l = \frac{d_l^2\rho_p}{18\mu}$). The normalized simulated time is 0–2.076. The liquid velocity at the inlet (0.10–0.20 m/s) is normalized by minimum fluidization velocity of species 2 (0.091 m/s). The normalized liquid velocity is 1.10–2.20. The liquid velocity and simulation time mentioned below refer to the normalized. Moreover, we consider the liquid velocity in excess of 1.65 as the high liquid velocity and not in excess of 1.65 as the low liquid velocity.

1. Layer inversion phenomenon

This part investigates the transient process of layer inversion at different liquid velocities. Initially, the layer of species 1 is on the bottom, and the species 2 forms the superposed layer. Figures 8 and 9 show the instantaneous state (0–1.245) of layer inversion at the liquid velocity of 1.54 and 1.98, respectively. The particles of species 2 are red, and the particles of species 1 are blue in the figure. In the initial

Downloaded from http://pubs.aip.org/aip/pof/article-pdf/doi/10.1063/5.0111157/16578096/103325_1_online.pdf

Published under an exclusive license by AIP Publishing

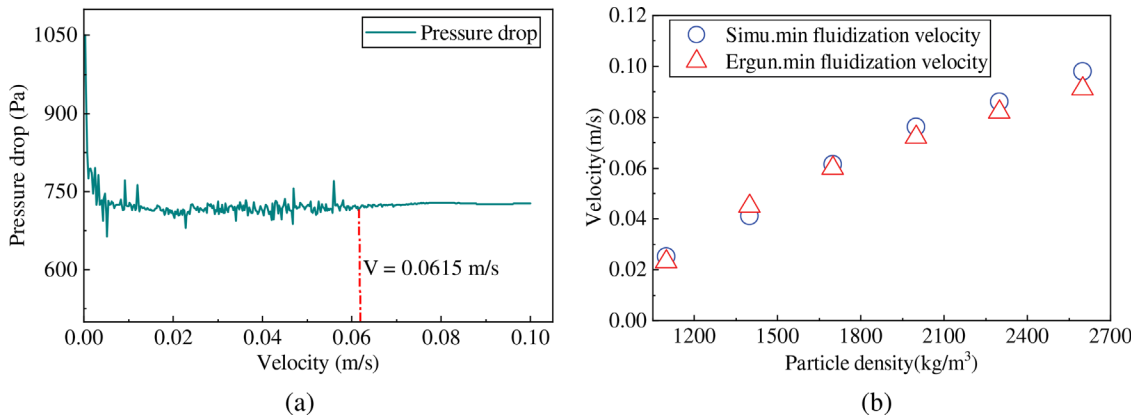

FIG. 6. Pressure drop verification between numerical simulation results and theoretical values of Ergun formula: (a) particle density and (b) fluid viscosity.

phase, the entire layer composed of species 1 and 2 rises as a granular plug with fluid flowing. With particles of species 1 falling off the bottom of the granular plug during the ascent process, the length of the granular plug decreases continuously. The initial stage finishes when the particles of species 2 also all fall completely. Then, the particles of species 1 that initially fall to the bottom of the pipe begin to migrate through the layer of species 2, and the particles of species 2 and particles of species 1 begin to mix. The level of mixture increases in the process of particles of species 1 rising. When the particles of species 1 eventually reach the top of species 2, the degree of mixing decreases and the layer inversion ends. As shown in Figs. 8 and 9, particles of species 1 begin to move upward even before the particles of species 2 all fall completely at a high liquid velocity (1.98). The granular plug rising in the initial stage is special in binary LSFBs with coarse particles, which is easy to cause pipe blockage. In Figs. 8 and 9, the ascending migration of species 1 is more rapid, and the inversion time of the layer is shorter at the liquid velocity of 1.98. This is because the drag force increases, causing the expansion height of the fluidized beds and the segregated degree of the species 1 and 2 to increase. The layer inversion phenomenon is the same as the experimental results,[45] but they did not analyze the reasons in depth. The specific layer inversion process is shown as the supplementary material.

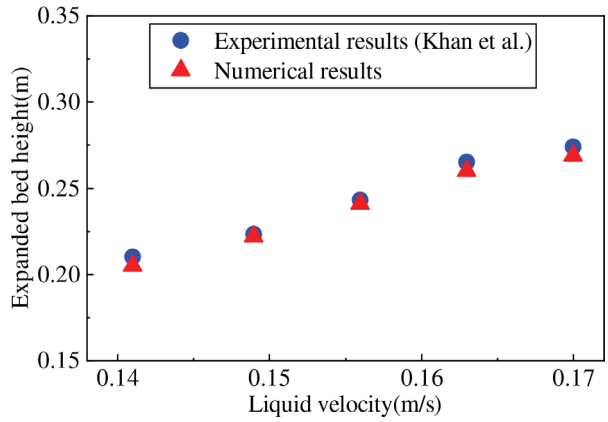

FIG. 7. Comparison of expansion height between numerical simulation and experiment.

2. Particle trajectories

The trajectory of single particle can better understand how the species 1 and 2 move, separate, and mix during the layer inversion. In this part, a particle of species 2 and a particle of species 1 are selected. The initial position of the species 1 is on the bottom of the pipe, and the species 2 is on the top of the species 1. Figure 10 shows the trajectories of species 1 and 2 at different liquid velocities (1.10, 1.21, 1.54, 1.76, 1.98, and 2.20). The horizontal and vertical directions are normalized by radius R and diameter D, respectively. The blue line corresponds to species 1, and the red line corresponds to species 2. In order to identify the trajectories of different time scales more clearly, the particle trajectories in normalized times 0–1.038 and 1.038–2.076 are represented by dashed lines and solid lines, respectively. For different liquid velocities, the particle of species 2 moves down to the bottom of the pipe, and the particle of species 1 moves up to the top of the particle of species 2. As shown in Fig. 10, the trajectory of the two species of particles is relatively simple at low liquid velocities (1.10, 1.21, and 1.54). Species 1 rises to the top of species 2 and wanders around thereafter on the top. Species 2 settles to the bottom and moves randomly. The trajectory of the two species of particles is complex and spans the whole bed at high liquid velocities (1.76, 1.98, and 2.20). Compared with the low liquid velocity, the travel distance of species 1 and 2 is longer at high liquid velocity.

3. Particle volume fraction

This part discusses the changes of particle volume fraction in the equilibrium along the horizontal and vertical directions of the pipe at different liquid velocities (1.32, 1.54, 1.76, 1.98, and 2.20). As shown in Fig. 11(a), the particle volume fraction increases first with the normalized height, then decreases, and, finally, decreases to 0 at different liquid velocities. The rate of decrease in the particle volume fraction is more rapid at low liquid velocities (1.32 and 1.54). However, the

Downloaded from http://pubs.aip.org/aip/pof/article-pdf/doi/10.1063/5.0111157/16578096/103325_1_online.pdf

Published under an exclusive license by AIP Publishing

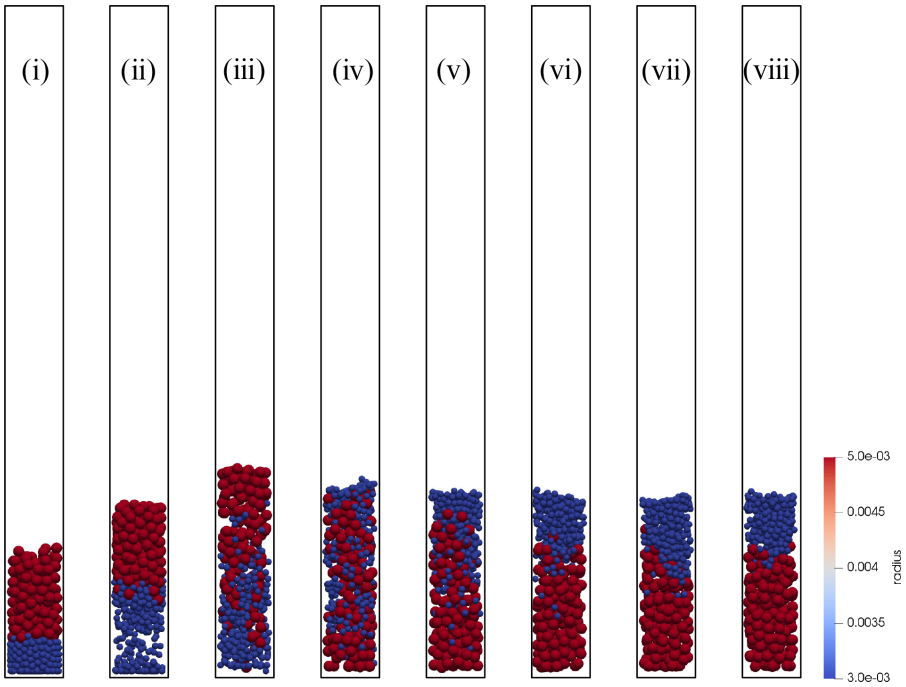

FIG. 8. Instantaneous snapshots of particle positions with the normalized liquid velocity of 1.54. The corresponding normalized times are (i) 0, (ii) 0.069, (iii) 0.208, (iv) 0.415, (v) 0.623, (vi) 0.830, (vii) 1.038, and (viii) 1.245.

particle volume fraction is relatively balanced at high liquid velocities (1.76 and 1.98) when the normalized height is between 0 and 3. When the liquid velocity is 2.20, the distribution of particle volume fraction with normalized height between 0 and 5 is more balanced. It is related to the decrease in particle collision frequency and increase in particle–fluid interaction force with the increase in liquid velocity. As shown in Fig. 11(b), the particle volume fraction of horizontal distance also decreases significantly with the increase in liquid velocity. Because the particles gather in the center and the upward fluid is blocked to flow to both sides, the particle volume fraction in the center of the pipe is slightly larger than that of the wall at different liquid velocities.

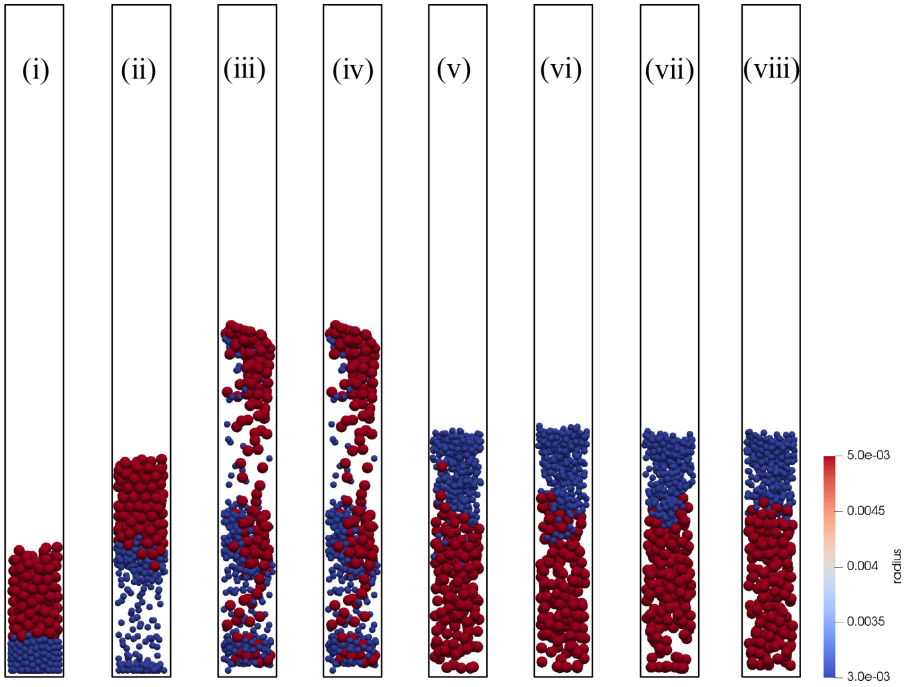

FIG. 9. Instantaneous snapshots of particle positions with the normalized liquid velocity of 1.98. The corresponding normalized times are (i) 0, (ii) 0.069, (iii) 0.208, (iv) 0.415, (v) 0.623, (vi) 0.830, (vii) 1.038, and (viii) 1.245.

Downloaded from http://pubs.aip.org/aip/pof/article-pdf/doi/10.1063/5.0111157/16578096/103325_1_online.pdf

Published under an exclusive license by AIP Publishing

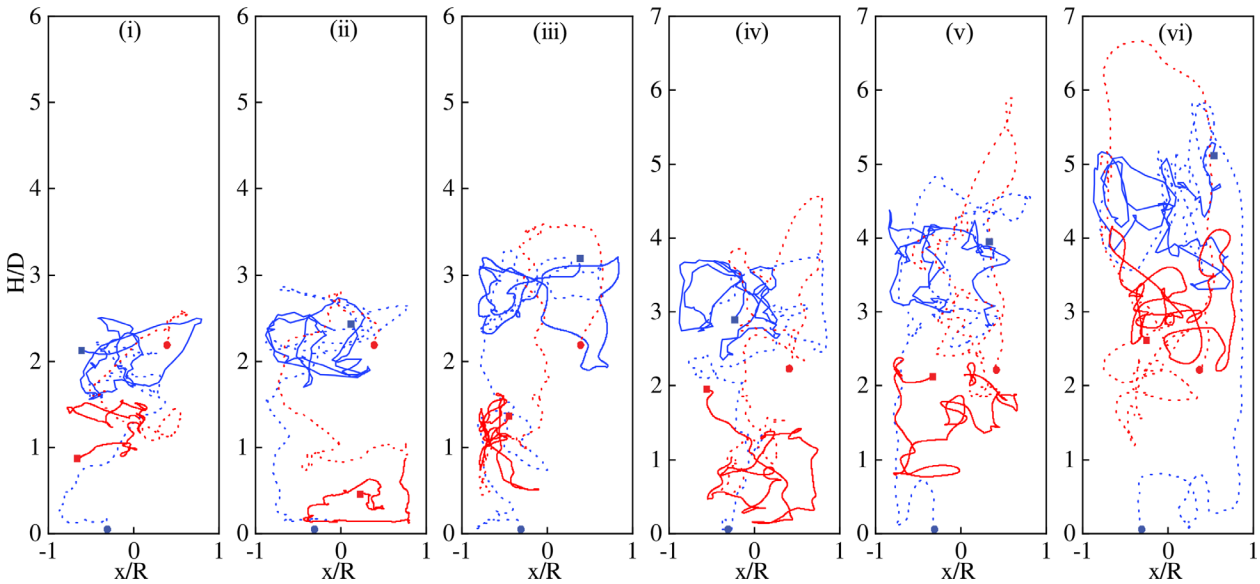

FIG. 10. The trajectories of species 1 (blue line) and 2 (red line) at different liquid velocities. The corresponding normalized velocities are (i) 1.21, (ii) 1.32, (iii) 1.54, (iv) 1.76, (v) 1.98, and (vi) 2.20.

C. Force analysis

This section mainly considers the particle–fluid interaction force ($\mathbf{F}_{pf}$), the particle–particle/wall interaction force ($\mathbf{F}_{col}$), and the total forces ($\mathbf{F}_s$) ($\mathbf{F}_s = \mathbf{F}_{pf} + \mathbf{F}_{col}$). Since the layer inversion with coarse particles occurs mainly in the vertical direction, the vertical component of these forces is mainly analyzed. These forces will be normalized by net gravity $\mathbf{f}_{g'} = (\rho_p - \rho_f)g$, and the vertical direction along the positive half-axis of the z-axis is specified as positive. The normalized "particle–fluid interaction force," "collision force," and "total force" are named "relative particle–fluid interaction force," "relative collision force," and "relative total force," respectively. The net gravity can also characterize the gravity of particles. The collision number of species 1 and 2 is normalized by their respective particle numbers, which is expressed as collision frequency.

1. The variation of forces over time

The changes in the relative particle–fluid interaction force and the relative particle–particle/wall interaction force over time are

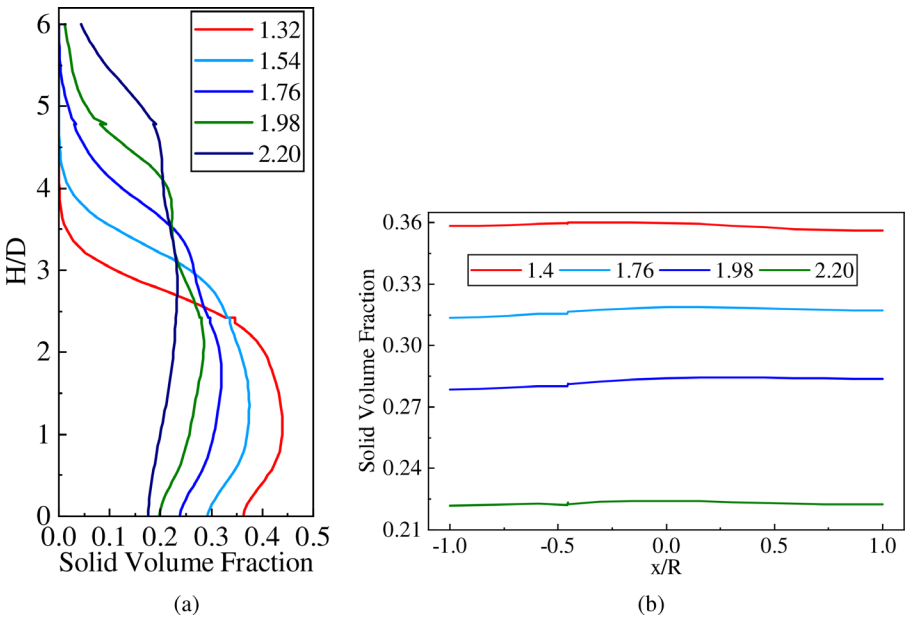

FIG. 11. Solid volume fraction at different normalized liquid velocities: (a) the evolution in the axial direction and (b) the evolution in the radial direction.

Downloaded from http://pubs.aip.org/aip/pof/article-pdf/doi/10.1063/5.0111157/16578096/103325_1_online.pdf

Published under an exclusive license by AIP Publishing

investigated. $\mathbf{F}_{\mathrm{pf},1} = \frac{\sum_{i=1}^{N} \mathbf{f}_{\mathrm{pf},i}}{N\mathbf{f}_{g'}}$, $\mathbf{F}_{\mathrm{p},1} = \frac{\sum_{i=1}^{N} \mathbf{f}_{\mathrm{p},i}}{N\mathbf{f}_{g'}}$, $\mathbf{F}_{\mathrm{pf},1}$ is the average value of the particle–fluid interaction force of species 1. $\mathbf{F}_{\mathrm{p},1}$ is the average value of the collision force between particles of species 1 and other particles or wall. $\mathbf{f}_{\mathrm{pf},i}$ is the force of fluid acting on the ith particle of species 1. $\mathbf{f}_{\mathrm{p},i}$ is the collision force between particle of species 1 i and other particles or wall.

As shown in Fig. 12, the relative particle–fluid interaction force, the relative particle–particle/wall interaction force, and collision frequency change over time at different liquid velocities (1.10, 1.54, and 1.98). As shown in Figs. 12(b) and 12(c), the relative particle–fluid interaction forces of species 1 and 2 are greater than 1 at the liquid velocities of 1.54 and 1.98 in the initial stage. Then, the relative interaction force between species 2 and the fluid is less than 1, but the relative force of the species 1 is always more than 1. It causes the particles of species 1 to migrate upward under the action of the fluid during the layer inversion. However, the force of fluid on species 2 is not sufficient to overcome the net gravity, which makes them settle down. Furthermore, when the liquid velocity is 1.54 and 1.98, the relative collision force of the species 1 is less than 0 and that of the species 2 is greater than 0. This means the collision force of species 2 is upward, and that of species 1 is downward at different liquid velocities. The change of these forces over time also explains the phenomenon of layer inversion in Figs. 8 and 9. As shown in Fig. 12(a), when the liquid velocity is 1.10, the normalized force curves of the relative particle–fluid interaction force between species 1 and species 2 are almost parallel. The collision frequency is much greater than those of other velocities, resulting in higher collision force. However, the collision force is almost zero after the normalized time 0.692 at the liquid velocities of 1.54 and 1.98. In addition, the layer inversion cannot occur at the liquid velocity of 1.10. Therefore, the collision force dominates in this case, so as to transfer energy to reach equilibrium.

2. The variation of forces with velocity

We also study the changes in the relative particle–fluid interaction force for species 1 and 2 at different liquid velocities (1.10–2.20). First, the time averages of the relative particle–fluid interaction force for species 1 and 2 in the equilibrium are calculated. Figure 13(a) shows the ratio of total forces ($\mathbf{f}_{\mathrm{pf}} + \mathbf{f}_{\mathrm{col}}$) on species 1 and 2 to the net gravity is about 1, indicating that the particles reach equilibrium. As shown in Fig. 13(b), the relative force of the fluid acting on the particles of species 1 is always greater than 1 at different liquid velocities, whereas the relative force acting on the particles of species 2 is less than 1. Corresponding to layer inversion phenomenon, the particle–fluid interaction force drives particles of species 1 to migrate upward, while the gravity causes particles of species 2 to sink during the layer inversion. Therefore, the relative magnitude of the fluid–solid interaction force and the gravity is the main reason for determining the layer inversion of binary coarse particles of different sizes.

As shown in Fig. 14(a), with the increase in liquid velocity, the relative drag force acting on particles increases and the relative pressure gradient force decreases. The drag force on species 1 is greater than that on species 2. Compared with drag and pressure gradient forces, the lift force for species 1 and 2 is of a small order of magnitude and can be ignored in Fig. 14(b).

The change in the relative particle–particle/wall interaction force for species 1 and 2 is investigated at different liquid velocities (1.10–2.20). As shown in Fig. 15(a), the relative collision force acting on species 2 is greater than 0, indicating that the direction of the force is upward. However, the relative collision force acting on small particles is less than 0, indicating that the direction of the force is downward. The collision force is mainly to compensate for the particle–fluid interaction force and the net gravity of particles, so that the particles are in relative equilibrium. As the liquid velocity increases, the fluidized bed expansion height increases. Figure 15(b) shows the collision frequency of particles decreases quickly, and the rate of

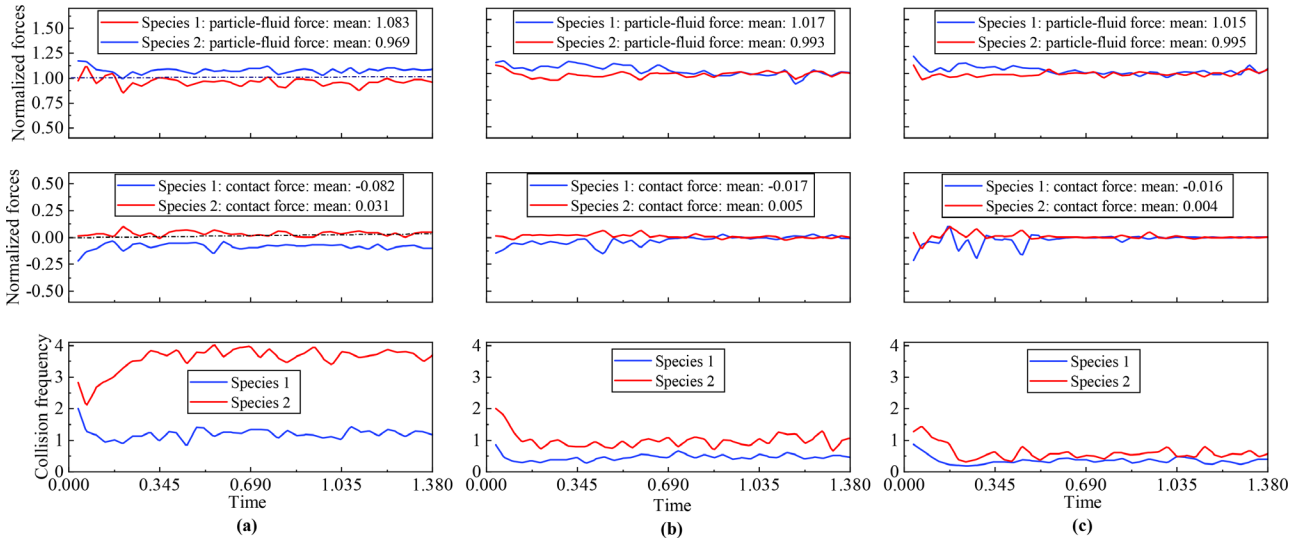

FIG. 12. The variation of the mean relative forces and collision frequency on both species 1 and 2: the first row is the relative particle–fluid interaction force. The second row is the relative particle–particle/wall interaction force. The last row is the particle–particle collision frequency. (a) 1.10, (b) 1.54, and (c) 1.98.

Downloaded from http://pubs.aip.org/aip/pof/article-pdf/doi/10.1063/5.0111157/16578096/103325_1_online.pdf

Published under an exclusive license by AIP Publishing

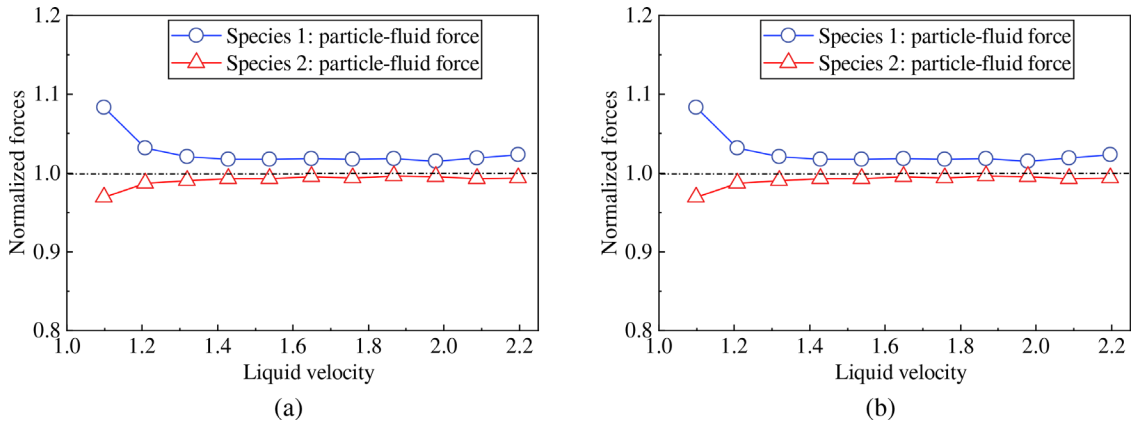

FIG. 13. Variation of the forces at different normalized liquid velocities: (a) the relative total forces and (b) the relative particle–fluid interaction force.

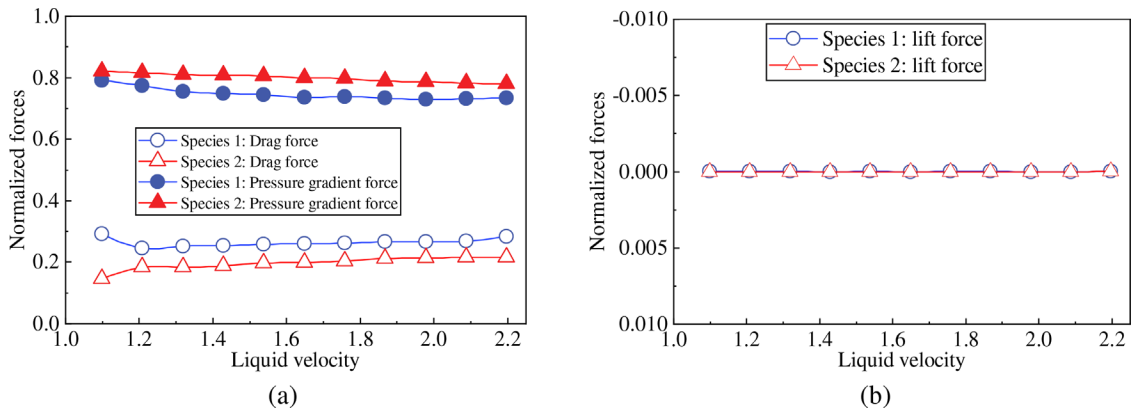

FIG. 14. Variations of mean relative forces with different normalized liquid velocities for species 1 and 2: (a) the relative drag force and pressure gradient force and (b) the relative lift force.

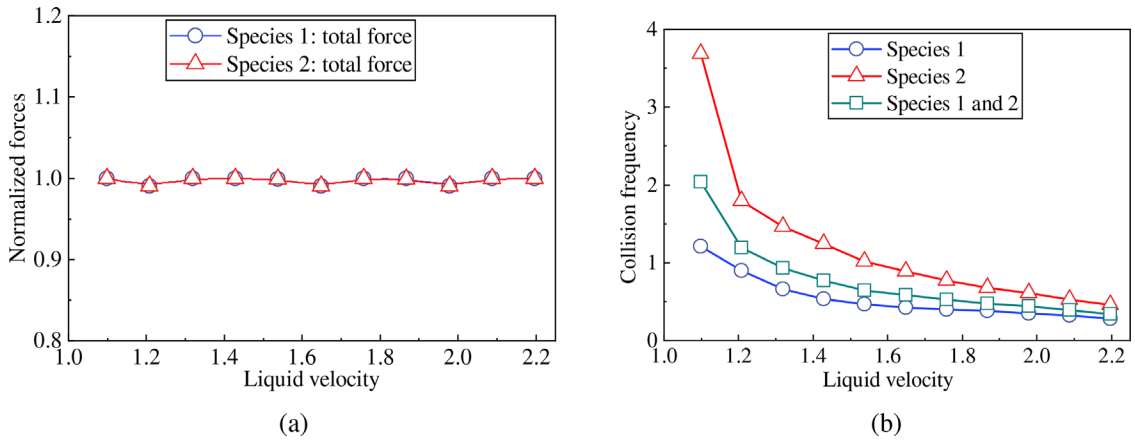

FIG. 15. Variations of mean relative collision forces and collision frequency with different normalized liquid velocities for species 1 and 2: (a) mean relative collision force and (b) mean collision frequency.

Downloaded from http://pubs.aip.org/aip/pof/article-pdf/doi/10.1063/5.0111157/16578096/103325_1_online.pdf

Published under an exclusive license by AIP Publishing

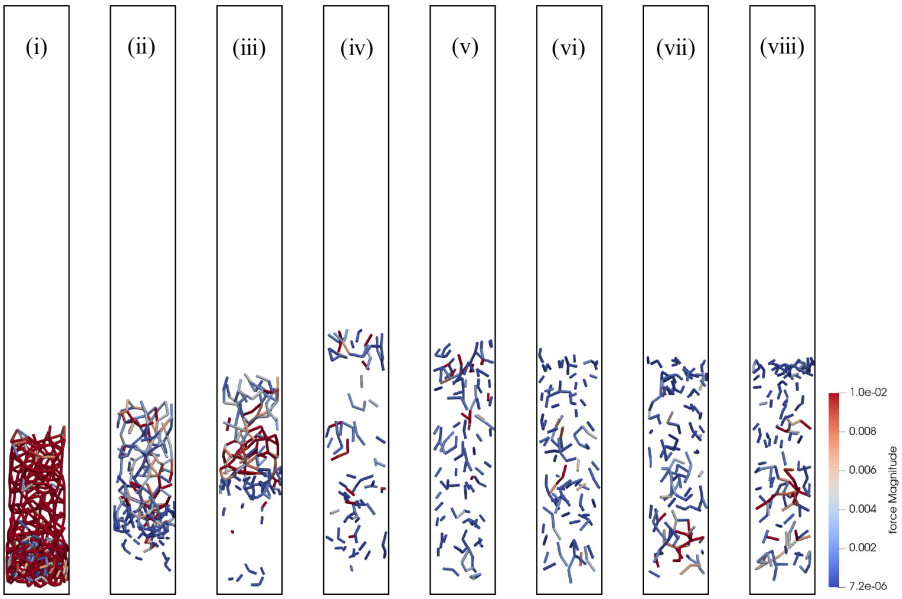

FIG. 16. Instantaneous snapshots of the network of contact forces and liquid velocity of 1.54. The corresponding normalized times are (i) 0, (ii) 0.035, (iii) 0.069, (iv) 0.208, (v) 0.346, (vi) 0.484, (vii) 0.623, and (viii) 0.761.

decrease in species 2 is significantly higher than that of species 1. The layer inversion cannot occur at the liquid velocity of 1.10, and the collision frequency of particles is higher than other velocities. Therefore, the collision force is dominant in the case and is coincidence with the result of Fig. 12(a).

3. The evolution of the network of contact force

Furthermore, in order to find out the influence of the wall on coarse particles during the layer inversion, we study the evolution of the network of contact forces at different liquid velocities (1.54 and 1.98). Figures 16 and 17 are the instantaneous snapshots of the evolution of the network of contact forces at 1.54 and 1.98, respectively. At the initial stage, compared to higher liquid velocity (1.98), the particle contact chains are denser and stronger at lower liquid velocity (1.54). It corresponds to the granular plug in the initial stages of Figs. 8 and 9 and also proves the constraint of the wall on the aggregation of coarse particles. Figure 17 shows the contact chains of coarse particles are obviously weakened at high liquid velocity (1.98), and the initial granular plug is also improved in Fig. 9. Therefore, an appropriate increase in liquid velocity helps to resolve granular plug of layer inversion at the initial stage, thereby reducing the probability of pipe blockage.

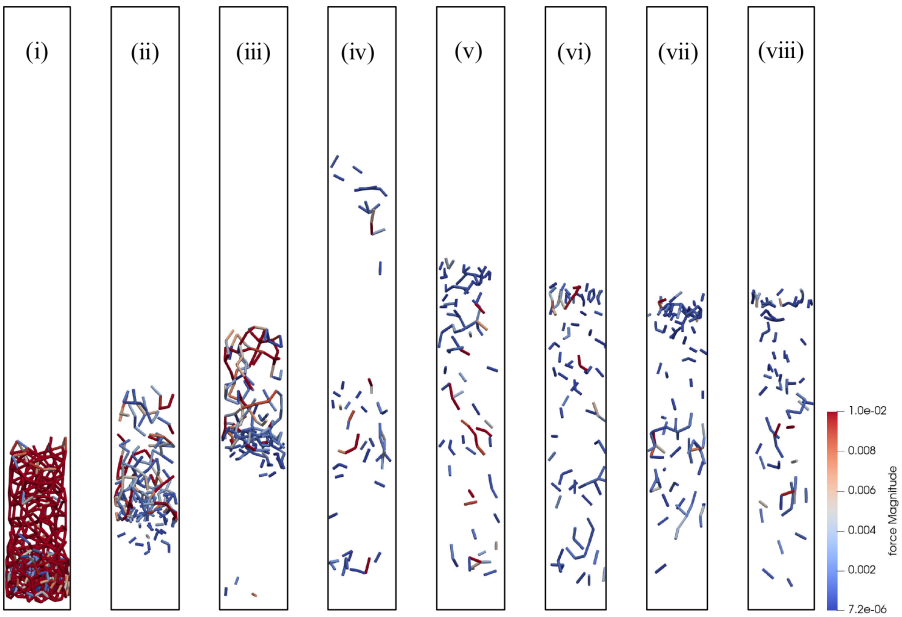

FIG. 17. Instantaneous snapshots of the network of contact forces and liquid velocity of 1.98. The corresponding normalized times are (i) 0, (ii) 0.035, (iii) 0.069, (iv) 0.208, (v) 0.346, (vi) 0.484, (vii) 0.623, and (viii) 0.761.

Downloaded from http://pubs.aip.org/aip/pof/article-pdf/doi/10.1063/5.0111157/16578096/103325_1_online.pdf

Published under an exclusive license by AIP Publishing

In summary, we quantitatively characterize the variation of two species of coarse particles trajectories and volume fractions and clarify the formation mechanisms of layer inversion with coarse particles. Moreover, the formation of granular plug is also discussed.

V. CONCLUSION

In this paper, the CFD–DEM model is used to study the characteristics and mechanisms of layer inversion in binary LSFBs with coarse particles. The model is based on an optimized Euler–Lagrange method proposed in our work, which solves the problem that the coarse particle size is larger than the mesh size. The qualitative and quantitative characteristics of the binary LSFBs layer inversion with coarse particles are studied. The particle–fluid interaction force and the particle–particle/wall interaction force are also taken into account to analyze the reason for layer inversion. Moreover, the influence of the wall on the coarse particles in binary LSFBs is discussed.

(i) The particle trajectory and the trajectory of the network of contact forces during layer inversion are obtained by numerical simulation. The results show that two species of coarse particles move upward as a granular plug at the initial state. Particles of species 1 are at the bottom of the pipe, and particles of species 2 are on the overlying layer in the initial stage. Finally, the phenomenon that the particles of species 2 are on the bottom and particles of species 1 are on the overlying layer forms. From the analysis of the evolution of the network of contact forces, the granular plug forms because of the strong restriction of the wall on coarse particles.

(ii) This paper also investigates the changes in trajectory and volume fraction of two species of particles in the process of layer inversion at different liquid velocities. The trajectory of particles is relatively simple at low liquid velocities (1.10, 1.32, and 1.54). The trajectory of particles is complex, and the trajectory spans the whole bed at high liquid velocities (1.76, 1.98, and 2.20). The particle volume fraction decreases rapidly along the bed height at low liquid velocity. However, the distribution of particle volume fraction is more uniform along the vertical direction at high liquid velocity. The particle volume fraction along the horizontal direction in the center of the pipe is slightly larger than that of the wall at different velocities.

(iii) The effects of the relative particle–fluid interaction force and the relative particle–particle/wall interaction force on the layer inversion are studied. The results show that the relative magnitude of the fluid–solid interaction force and the gravity is the main reason for determining the layer inversion of binary coarse particles of different sizes. The collision force is to balance the net force of the particle–fluid interaction force and the net gravity, so that the fluidized bed is in relative equilibrium. With the increase of liquid velocity, the drag force acting on particles increases and the pressure gradient force decreases. The lift force acting on particles has little effect. With the increase of liquid velocity, the collision frequency of two species of particles decreases, but the collision frequency of species 2 decreases faster.

SUPPLEMENTARY MATERIAL

See the supplementary material for the GIF diagrams of the layer inversion process and the change of the network of contact forces when the normalized fluid velocities are 1.54 and 1.98, respectively.

ACKNOWLEDGMENTS

This study was supported by the Strategic Priority Research Program of the Chinese Academy of Sciences (Grant No. XDA22000000), the National Natural Science Foundation of China (Grant No. 12132018), and the Youth Innovation Promotion Association of Chinese Academy of Sciences (No. 2017027).

AUTHOR DECLARATIONS

Conflict of Interest

The authors have no conflicts to disclose.

Author Contributions

Wanlong Ren: Conceptualization (equal); Data curation (lead); Formal analysis (lead); Methodology (equal); Software (equal); Validation (equal); Writing – original draft (lead); Writing – review & editing (equal). **Yan Zhang:** Methodology (equal); Software (equal); Supervision (lead); Writing – review & editing (equal). **Xuhui Zhang:** Conceptualization (lead); Funding acquisition (lead); Methodology (equal); Writing – review & editing (lead). **Xiaobing Lu:** Conceptualization (equal); Supervision (equal); Writing – review & editing (equal).

DATA AVAILABILITY

The data that support the findings of this study are available from the corresponding author upon reasonable request.

APPENDIX: THE ERGUN FORMULA

The Ergun formula is as follows:

$$\begin{gathered}(Re)_{\mathrm{p}} < 20 \\ \mathbf{U}_{\mathrm{mf}} = \frac{(\Phi_{\mathrm{p}} d)^2 (\rho_{\mathrm{p}} - \rho_{\mathrm{f}}) g}{150\mu} \times \frac{\varepsilon_{\mathrm{f}}^3}{1-\varepsilon_{\mathrm{f}}}, \\ 20 < (\mathrm{Re})_p < 1000 \\ \frac{1.75(\Phi_{\mathrm{p}} d)\rho_{\mathrm{p}}}{\mu \varepsilon_{\mathrm{f}}^3} \mathbf{U}_{\mathrm{mf}}^2 + 150 \frac{1-\varepsilon_{\mathrm{f}}}{\varepsilon_{\mathrm{f}}^3} \mathbf{U}_{\mathrm{mf}} = \frac{(\Phi_{\mathrm{p}} d)^2 (\rho_{\mathrm{p}} - \rho_{\mathrm{f}}) g}{\mu}, \\ (Re)_p > 1000 \\ \mathbf{U}_{\mathrm{mf}} = \left(\frac{\Phi_{\mathrm{p}} d (\rho_{\mathrm{p}} - \rho_{\mathrm{f}}) g}{1.75 \rho_{\mathrm{f}}} \varepsilon_{\mathrm{f}}^3 \right)^{0.5},\end{gathered} \tag{A1}$$

where $(Re)_{\mathrm{p}} = \frac{\mathbf{U}_{\mathrm{f}} d \rho_{\mathrm{p}}}{\mu}$ is the particle Reynolds number, ρ_{p} is the particle density, ρ_{f} is the fluid density, μ is the fluid viscosity, ϕ_{p} is the sphericity, ε_{f} is the volume fraction of the fluid, and $\mathbf{U}_{\mathrm{mf}}$ is the minimum fluidization velocity.

REFERENCES

[1] R. F. Hoffman, L. Lapidus, and J. Elgin, "The mechanics of vertical moving fluidized systems: IV. Application to batch-fluidized systems with mixed particle sizes," AIChE J. **6**, 321–324 (1960).

Downloaded from http://pubs.aip.org/aip/pof/article-pdf/doi/10.1063/5.0111157/16578096/103325_1_online.pdf

Published under an exclusive license by AIP Publishing

[2]N. Epstein, B. Leclair, and B. Pruden, "Liquid fluidization of binary particle mixtures—I: Overall bed expansion," Chem. Eng. Sci. **36**, 1803–1809 (1981).
[3]N. Epstein, "Applications of liquid-solid fluidization," Int. J. Chem. React. Eng. **1**, 1–16 (2002).
[4]P. V. Chavan and J. B. Joshi, "Analysis of particle segregation and intermixing in solid-liquid fluidized beds," Ind. Eng. Chem. Res. **47**, 8458–8470 (2008).
[5]N. Epstein, "Teetering," Powder Technol. **151**, 2–14 (2005).
[6]R. Hancock, "The teeter condition," Min. Mag. **55**, 90–94 (1936).
[7]R. Di Felice, L. Gibilaro, and P. Foscolo, "On the inversion of binary-solid liquid fluidised beds," Chem. Eng. Sci. **43**, 979–981 (1988).
[8]A. Kumari, A. Tripathy, and V. Rayasam, "Performance characterization and misplacement studies of liquid–solid fluidized bed density separator for coal beneficiation using Taguchi-ANOVA method," Part. Sci. Technol. **39**, 436–448 (2021).
[9]R. Escudie, N. Epstein, J. R. Grace, and H. T. Bi, "Layer inversion phenomenon in binary-solid liquid-fluidized beds: Prediction of the inversion velocity," Chem. Eng. Sci. **61**, 6667–6690 (2006).
[10]F. P. Di Maio and A. Di Renzo, "Direct modeling of voidage at layer inversion in binary liquid-fluidized bed," Chem. Eng. J. **284**, 668–678 (2016).
[11]M. Syamlal and T. O'brien, "Simulation of granular layer inversion in liquid fluidized beds," Int. J. Multiphase Flow **14**, 473–481 (1988).
[12]A. Mukherjee and B. Mishra, "Experimental and simulation studies on the role of fluid velocity during particle separation in a liquid–solid fluidized bed," Int. J. Miner. Process. **82**, 211–221 (2007).
[13]H. Moritomi, T. Iwase, and T. Chiba, "A comprehensive interpretation of solid layer inversion in liquid fluidised beds," Chem. Eng. Sci. **37**, 1751–1757 (1982).
[14]N. Epstein and B. LeClair, "Liquid fluidization of binary particle mixtures—II. Bed inversion," Chem. Eng. Sci. **40**, 1517–1526 (1985).
[15]J. Richardson and W. Zaki, "Sedimentation and fluidisation: Part I," Trans. Inst. Chem. Eng. **32**, S82–S100 (1954).
[16]X. Hu, "Prediction of the inversion velocity in the binary-solid liquid fluidized bed," Chem. Eng. Sci. **57**, 3149–3153 (2002).
[17]L. Gibilaro, R. Di Felice, S. Waldram, and P. Foscolo, "A predictive model for the equilibrium composition and inversion of binary-solid liquid fluidized beds," Chem. Eng. Sci. **41**, 379–387 (1986).
[18]M. Asif, "The complete segregation model for a liquid fluidized bed: Formulation and related issues," Powder Technol. **140**, 21–29 (2004).
[19]A. Khan and J. Richardson, "Fluid-particle interactions and flow characteristics of fluidized beds and settling suspensions of spherical particles," Chem. Eng. Commun. **78**, 111–130 (1989).
[20]A. Di Renzo, G. Rito, and F. P. Di Maio, "Systematic experimental investigation of segregation direction and layer inversion in binary liquid-fluidized bed," Processes **8**, 177 (2020).
[21]G. Rim, C. Jeong, J. Bae, Y. Lee, D. H. Lee, N. Epstein, J. R. Grace, and S. D. Kim, "Prediction of layer inversion velocity in three-phase fluidized beds," Chem. Eng. Sci. **100**, 91–97 (2013).
[22]Y. Zhang, X.-B. Lu, and X.-H. Zhang, "Numerical simulation on transportation behavior of dense coarse particles in vertical pipe with an optimized Eulerian–Lagrangian method," Phys. Fluids **34**, 033305 (2022).
[23]B. Viggiano, O. Skjæraasen, H. Schümann, M. Tutkun, and R. B. Cal, "Characterization of flow dynamics and reduced-order description of experimental two-phase pipe flow," Int. J. Multiphase Flow **105**, 91–101 (2018).
[24]N. Ali, B. Viggiano, M. Tutkun, and R. B. Cal, "Cluster-based reduced-order descriptions of two phase flows," Chem. Eng. Sci. **222**, 115660 (2020).
[25]N. Ali, B. Viggiano, M. Tutkun, and R. B. Cal, "Data-driven machine learning for accurate prediction and statistical quantification of two phase flow regimes," J. Pet. Sci. Eng. **202**, 108488 (2021).
[26]D. A. Drew, "Mathematical modeling of two-phase flow," Annu. Rev. Fluid Mech. **15**, 261–291 (1983).
[27]R. K. Reddy and J. B. Joshi, "CFD modeling of solid–liquid fluidized beds of mono and binary particle mixtures," Chem. Eng. Sci. **64**, 3641–3658 (2009).
[28]M. S. Khan, G. M. Evans, Z. Peng, E. Doroodchi, B. Moghtaderi, J. B. Joshi, and S. Mitra, "Expansion behaviour of a binary solid-liquid fluidised bed with different solid mass ratio," Adv. Powder Technol. **28**, 3111–3129 (2017).
[29]S. Wang, Z. Sun, X. Li, J. Gao, X. Lan, and Q. Dong, "Simulation of flow behavior of particles in liquid–solid fluidized bed with uniform magnetic field," Powder Technol. **237**, 314–325 (2013).
[30]M. Chiesa, V. Mathiesen, J. A. Melheim, and B. Halvorsen, "Numerical simulation of particulate flow by the Eulerian–Lagrangian and the Eulerian–Eulerian approach with application to a fluidized bed," Comput. Chem. Eng. **29**, 291–304 (2005).
[31]E. A. Molaei, A. Yu, and Z. Zhou, "Particle scale modelling of solid flow characteristics in liquid fluidizations of ellipsoidal particles," Powder Technol. **338**, 677–691 (2018).
[32]Y. Yao, C. S. Criddle, and O. B. Fringer, "The effects of particle clustering on hindered settling in high-concentration particle suspensions," J. Fluid Mech. **920**, A40 (2021).
[33]Y. Yao, C. S. Criddle, and O. B. Fringer, "Competing flow and collision effects in a monodispersed liquid–solid fluidized bed at a moderate Archimedes number," J. Fluid Mech. **927**, A28 (2021).
[34]F. D. Cúñez, N. C. Lima, and E. M. Franklin, "Motion and clustering of bonded particles in narrow solid–liquid fluidized beds," Phys. Fluids **33**, 023303 (2021).
[35]F. Cello, A. Di Renzo, and F. P. Di Maio, "DEM-CFD simulations of layer inversion in two-component liquid fluidized beds," Chem. Eng. Trans. **17**, 627–632 (2009).
[36]A. Di Renzo, F. Cello, and F. P. Di Maio, "Simulation of the layer inversion phenomenon in binary liquid–fluidized beds by DEM–CFD with a drag law for polydisperse systems," Chem. Eng. Sci. **66**, 2945–2958 (2011).
[37]V. Vivacqua, S. Vashisth, G. Hébrard, J. Grace, and N. Epstein, "Characterization of fluidized bed layer inversion in a 191-mm-diameter column using both experimental and CPFD approaches," Chem. Eng. Sci. **80**, 419–428 (2012).
[38]Z. Peng, J. B. Joshi, B. Moghtaderi, M. S. Khan, G. M. Evans, and E. Doroodchi, "Segregation and dispersion of binary solids in liquid fluidised beds: A CFD-DEM study," Chem. Eng. Sci. **152**, 65–83 (2016).
[39]Z. Xie, S. Wang, and Y. Shen, "CFD-DEM study of segregation and mixing characteristics under a bi-disperse solid-liquid fluidised bed," Adv. Powder Technol. **32**, 4078–4095 (2021).
[40]B. Viggiano, J. Friedrich, R. Volk, M. Bourgoin, R. B. Cal, and L. Chevillard, "Modelling Lagrangian velocity and acceleration in turbulent flows as infinitely differentiable stochastic processes," J. Fluid Mech. **900**, A27 (2020).
[41]J. Friedrich, B. Viggiano, M. Bourgoin, R. B. Cal, and L. Chevillard, "Single inertial particle statistics in turbulent flows from Lagrangian velocity models," Phys. Rev. Fluids **7**, 014303 (2022).
[42]K. F. Malone, B. H. Xu, and M. Fairweather, "Numerical investigation of the layer-inversion phenomenon in binary solid liquid fluidized beds," in 12th International Conference on Fluidization-New Horizons in Fluidization, 2007.
[43]Z. Zhou and A. Yu, "Simulation of the flow and segregation of particle mixtures in liquid fluidization," AIP Conf. Proc. **1145**, 993–996 (2009).
[44]E. A. Molaei, A. Yu, and Z. Zhou, "Investigation of causes of layer inversion and prediction of inversion velocity in liquid fluidizations of binary particle mixtures," Powder Technol. **342**, 418–432 (2019).
[45]F. D. Cúñez and E. M. Franklin, "Mimicking layer inversion in solid-liquid fluidized beds in narrow tubes," Powder Technol. **364**, 994–1008 (2020).
[46]F. D. Cúñez and E. M. Franklin, "Crystallization and jamming in narrow fluidized beds," Phys. Fluids **32**, 083303 (2020).
[47]Z. Peng, E. Doroodchi, C. Luo, and B. Moghtaderi, "Influence of void fraction calculation on fidelity of CFD-DEM simulation of gas-solid bubbling fluidized beds," AIChE J. **60**, 2000–2018 (2014).
[48]Y. Zhang, X.-B. Lu, and X.-H. Zhang, "An optimized Eulerian–Lagrangian method for two-phase flow with coarse particles: Implementation in open-source field operation and manipulation, verification, and validation," Phys. Fluids **33**, 113307 (2021).
[49]C. Kloss, C. Goniva, A. Hager, S. Amberger, and S. Pirker, "Models, algorithms and validation for opensource DEM and CFD–DEM," Prog. Comput. Fluid Dyn. **12**, 140–152 (2012).
[50]C. Kloss, C. Goniva, and S. Pirker, "Open source DEM and CFD-DEM with LIGGGHTS and OpenFOAM," in Open Source CFD International Conference, 2010.
[51]C. Kloss and C. L. Goniva, "LIGGGHTS - A new open source discrete element simulation software," in *Proceedings of 5th International Conference on Discrete Element Methods* (London, 2010), pp. 25–26. ISBN: 978-0-9551179-8-5.

Downloaded from http://pubs.aip.org/aip/pof/article-pdf/doi/10.1063/5.0111157/16578096/103325_1_online.pdf

Published under an exclusive license by AIP Publishing

[52]P. Sippola, J. Kolehmainen, A. Ozel, X. Liu, P. Saarenrinne, and S. Sundaresan, "Experimental and numerical study of wall layer development in a tribo-charged fluidized bed," J. Fluid Mech. **849**, 860–884 (2018).
[53]J. Zhao, S. Chen, K. Zhang, and Y. Liu, "A review of many-body dissipative particle dynamics (mdpd): Theoretical models and its applications," Phys. Fluids **33**, 112002 (2021).
[54]P. A. Cundall and O. D. Strack, "A discrete numerical model for granular assemblies," Geotechnique **29**, 47–65 (1979).
[55]Y. Tsuji, T. Tanaka, and T. Ishida, "Lagrangian numerical simulation of plug flow of cohesionless particles in a horizontal pipe," Powder Technol. **71**, 239–250 (1992).
[56]Z. Zhou, S. Kuang, K. Chu, and A. Yu, "Discrete particle simulation of particle–fluid flow: Model formulations and their applicability," J. Fluid Mech. **661**, 482–510 (2010).
[57]R. Zhao, Y. Zhou, D. Zhang, and X. Gao, "Numerical investigation of the hydraulic transport of coarse particles in a vertical pipe based on a fully-coupled numerical model," Int. J. Multiphase Flow **155**, 104094 (2022).
[58]Y. Jiang, Y. Guo, Z. Yu, X. Hua, J. Lin, C. R. Wassgren, and J. S. Curtis, "Discrete element method–computational fluid dynamics analyses of flexible fibre fluidization," J. Fluid Mech. **910**, A8 (2021).
[59]D. Gidaspow, *Multiphase Flow and Fluidization: Continuum and Kinetic Theory Descriptions* (Academic Press, 1994).
[60]S. Ergun, "Fluid flow through packed columns," Chem. Eng. Prog. **48**, 89–94 (1952).
[61]C. Wen and Y. Yu, "A generalized method for predicting the minimum fluidization velocity," AIChE J. **12**, 610–612 (1966).
[62]S. I. Rubinow and J. B. Keller, "The transverse force on a spinning sphere moving in a viscous fluid," J. Fluid Mech. **11**, 447–459 (1961).
[63]Y. Li, Y. Xu, and C. Thornton, "A comparison of discrete element simulations and experiments for 'sandpiles' composed of spherical particles," Powder Technol. **160**, 219–228 (2005).
[64]M. S. Khan, S. Mitra, S. Ghatage, Z. Peng, E. Doroodchi, B. Moghtaderi, J. B. Joshi, and G. M. Evans, "Pressure drop and voidage measurement in solid-liquid fluidized bed: Experimental, mathematical and computational study," in *Chemeca 2016: Chemical Engineering-Regeneration, Recovery and Reinvention* (Engineers Australia, Melbourne, VIC, 2016), pp. 1019–1030.
[65]Z. Wang, H. Wang, K. Luo, and J. Fan, "Direct numerical simulation of particle-laden turbulent boundary layers without and with combustion," Phys. Fluids **32**, 105108 (2020).
[66]G. Chen, H. Wang, K. Luo, and J. Fan, "Two-way coupled turbulent particle-laden boundary layer combustion over a flat plate," J. Fluid Mech. **948**, A12 (2022).

Downloaded from http://pubs.aip.org/aip/pof/article-pdf/doi/10.1063/5.0111157/16578096/103325_1_online.pdf

Published under an exclusive license by AIP Publishing